JTTEE5 13:554-560
DOI: 10.1361/10599630421488
1059-9630/$19.00 © ASM International

Peer Reviewed

Numerical Modeling of Short Crack Behavior in a Thermal Barrier Coating Upon Thermal Shock Loading

Y. Liu, C. Persson, and S. Melin

(Submitted July 1, 2003; in revised form September 15, 2003)

The behavior of microstructurally short inherent cracks within a preoxidized thermal barrier coating system upon thermal shock loading is considered. A thin alumina oxide layer holding residual stresses was induced at the ceramic/metal interface to simulate thermally grown oxide on the bond coat. Undulation of the oxidized bond coat was modeled as a sinusoidal surface. The variations of the stress-intensity factors of inherent centrally located cracks and of edge cracks were calculated during the thermal cycling. The instant crack shapes during the first thermal cycle and at steady state were investigated. It was found that oxide layer thickness, crack tip location, as well as interfacial undulation are factors influencing the risk of crack propagation. It was also found that an edge crack constitutes a greater threat to the coating durability than a central crack. The propagation of an edge crack, if it occurs, will take place during the first load cycle, whereas for a central crack, crack tip position decides the risk of crack propagation.

Keywords crack closure, finite element modeling, short cracks, thermal barrier coating, thermally grown oxide

1. Introduction

Conventional plasma-sprayed thermal barrier coatings (TBCs), consisting of an yttria partially stabilized zirconia ceramic topcoat and a metallic bond coat, are frequently used to provide thermal insulation to hot engine components in, for example, gas turbines to enhance engine efficiency during service. Local failure of the coating inevitably leads to a global malfunction of the gas turbine in that the protection of the metal against extreme temperature decays.

The most commonly reported failure mechanism of plasma-sprayed and low-pressure plasma-spayed TBCs in service under thermal cyclic loading is delamination followed by spallation as a result of in-plane cracking in the ceramic topcoat adjacent to the ceramic/metal interface (Ref 1, 2). Such a delamination crack is clearly seen in Fig. 1. The main causes behind delamination are residual stresses building up during thermal cycling due to thermal expansion mismatches among different layers in the coating system, nonelastic deformation of the bond coat, inherent short cracks in the topcoat, and the influence of thermally grown oxides (TGOs) on the bond coat at the ceramic/metal interface as discussed by DeMasi et al. (Ref 3) and Miller and Lowell (Ref 4). DeMasi et al. (Ref 3) reported that little evidence of significant, direct oxide-induced ceramic crack initiation could be found despite extensive metallographic examinations. It was thus assumed that fracture is initiated through a process of the growth of preexisting short cracks that are inherent in the coating from the manufacturing process.

The objective of this study was to investigate the behavior of and the risk for fracture from short inherent cracks in the topcoat upon thermal cyclic loading. In a previous work by the authors (Ref 5), modeling of a narrow slice of a standard Volvo TBC system with inherent central short cracks was conducted using the finite-element method. The risk of the propagation of stationary, preexisting central cracks near the interface in as-sprayed as well as in preoxidized TBC systems due to cyclic thermal shock loading was investigated, taking into account the influence of the TGOs and the nonelasticity of the bond coat on the coating system. It was found that the short cracks in the as-sprayed TBC system showed a higher risk of propagation if the crack tip position was above an apex compared with a crack tip position above a valley of the rough interface. In preoxidized TBCs, the trend is the opposite. In this study, the whole TBC system subjected to thermal shock tests was modeled, and the behavior of preexisting centrally positioned cracks as well as of edge cracks was investigated and compared. The roughness of the interface, the residual stresses in the TGO, the nonlinear temperature-dependent material properties, and the eventual contact between the crack surfaces were accounted for.

2. Numerical Modeling

The TBC system under consideration was a standard coupon sample (Volvo Aero Corporation, Trollhättan, Sweden), consisting of a Hastelloy substrate coated with a Ni-23Co-17Cr-12.5Al-0.5Y (wt.%) bond coat and a topcoat of $ZrO_2$7.5wt.%-Y_2O_3. The rough interface between the topcoat and the bond coat held an oxide layer, which was assumed to be Al_2O_3. The material parameters varied with temperature and are, for the different layers at 700 °C, listed in Table 1. The topcoat and the oxide layer were both modeled as elastic material. The bond coat and

Y. Liu and **C. Persson,** Division of Materials Engineering, Department of Mechanical Engineering, Lund University, SE-22100, Lund, Sweden; and **S. Melin,** Division of Solid Mechanics, Department of Mechanical Engineering, Lund University, SE-22100, Lund, Sweden. Contact e-mail: yan.liu@material.lth.se.

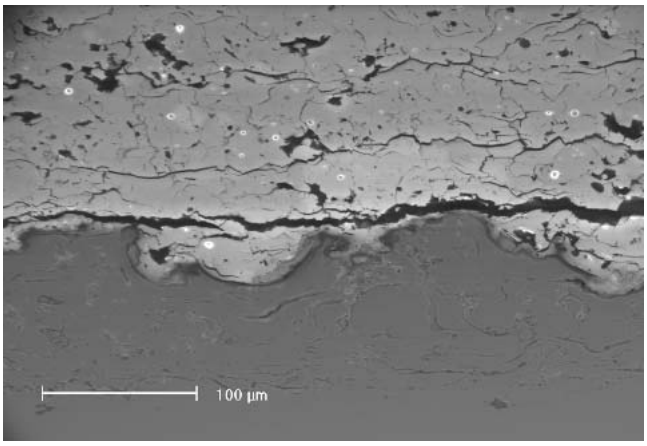

Fig. 1 Microstructure including a delamination crack in the ceramic topcoat adjacent to the interface

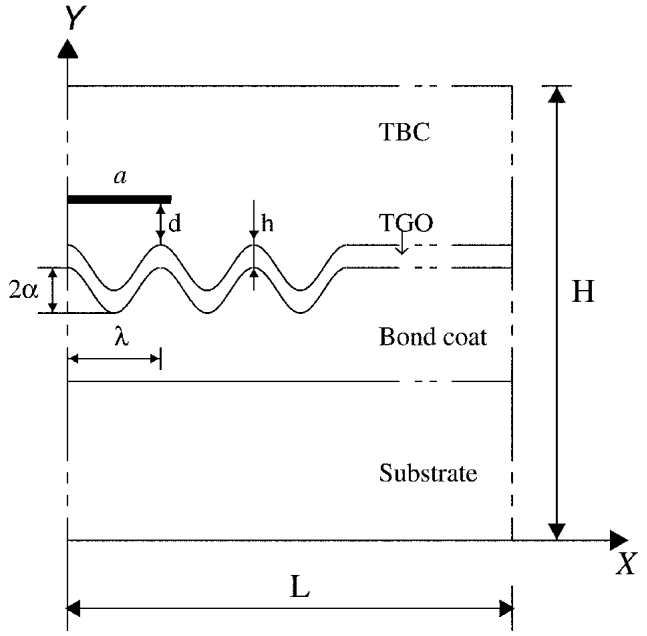

Fig. 2 Geometry of the TBC system

the substrate were modeled as elastic-viscoplastic material, obeying the von Mises yield criterion for perfect plasticity and the Norton creep law.

The model geometry, corresponding to the cross section of the sample, is depicted in Fig. 2. The width of the model (L) equaled the sample diameter of 25.4 mm that was used in the experiments. The height (H) of the sample was 7.3 mm. The average thickness of the topcoat was 0.45 mm, and that of the bond coat was 0.09 mm. The rough, wavy interface was modeled sinusoidally with wavelength $\lambda = 110$ μm and amplitude $2\alpha = 25$ μm, as estimated from experiments (Ref 2). The wavy interface extends for three wavelengths and is thereafter smoothened into a planar surface to simplify the model. The thickness (h) of the oxide layer was set to either 3 or 6 μm. A stationary, preexisting sharp crack was introduced a distance $d = 10$ μm above an asperity of the interface, in parallel with the global direction of the interface. Either a central crack or an edge crack was modeled, as determined from the boundary conditions. For a central crack, the y-axis is the axis of symmetry, whereas for an edge crack the side of the cross section along the y-axis corresponds to the free edge. The total crack length is a for an edge crack and $2a$ for a central crack due to symmetry, with a varying between 5 and 180 μm.

Table 1 Material properties for different layers at 700 °C

Layers	Ceramic coat	Al_2O_3	Bond coat	Substrate
Modulus of elasticity (E), GPa	17	345	103	150
Poisson's ratio	0.20	0.32	0.27	0.30
Yield stress, MPa	…	…	95	270
CTE, $\times 10^{-6}$/°C	11.00	7.79	15.00	15.00
Creep behavior(a)	…	…	A = 2.04e-34 B = 3.35	A = 3.18e-56 B = 6.00

Note: CTE, coefficient of thermal expansion. (a) Defined by the relation $\dot{\epsilon} = A\sigma^B$, where $\dot{\epsilon}$ is the strain rate in units of s^{-1}, A is the creep coefficient in units of (MPa)-B s^{-1}, σ is the effective von Mises stress in MPa, and B the dimensionless creep exponent. Source: Ref 1, 2

The system was subjected to cyclic thermal loading, with the temperature cycling between 400 and 930 °C with a period of 150 s following the experimental setup (Ref 2). Finite-element software (ABAQUS, Pautucket, RI) (Ref 6) was used to perform the calculations in two steps: a thermal analysis followed by a mechanical analysis, with the calculated node temperatures from the thermal analysis used as input for the mechanical analysis.

In the thermal analysis, the heat flux in through the upper boundary ($Y = H$) and out of the lower boundary ($Y = 0$) of the sample were, for each geometrical configuration, determined by an iterative procedure, resulting in a maximum discrepancy between the simulated temperatures and the experimental measurements within 2% (Ref 2). Figure 3 depicts the first few temperature cycles, with the three curves showing the simulated temperatures at the topcoat surface ($Y = H$), at the substrate backside ($Y = 0$), and at a point along the crack plane far from the crack tip.

In the mechanical analysis, generalized plane strain conditions were assumed, and 1071 biquadratic elements modeled the geometry. Contact elements were introduced between the crack surfaces to avoid overlap and to provide the possibility of inducing Coulomb friction between the crack surfaces whenever they were in contact. The square root singularity at the crack tip was modeled through focusing the mesh at the crack tip and moving the midside nodes of the elements surrounding the tip to the quarter points (Ref 7). The mode I and mode II stress-intensity factors K_I and K_{II} at the crack tip were calculated continuously during the thermal cycling from the displacements at the nodes closest to the crack tip. The simulations were pursued until steady state was reached, with steady state defined as prevailing when the maximum and minimum values of both K_I and K_{II} varied less than 0.1% between consecutive load cycles.

The residual stresses in the oxide layer were accounted for by imposing initial strains in the layer, with the initial strains chosen to induce an average hydrostatic stress of magnitude –1.4 GPa above the apices and of magnitude –1.8 GPa in the valleys of the oxide layer, in agreement with the measurements by Wright et al. (Ref 8).

3. Results and Discussion

Figure 4(a) shows the maximum and minimum value of K_I at the tip of a centrally situated crack during the first load cycle (K^1_{Imax} and K^1_{Imin}) and at steady state (K^{ss}_{Imax} and K^{ss}_{Imin}). The half-crack length is a, with a in the interval 5 μm < a < 180 μm. The calculated values are connected with solid lines in the diagram. Figure 4(b) shows the corresponding values for K_{II}. The results obtained for an edge crack of length a, with 5 μm < a < 180 μm, are shown in Fig. 5. Both Fig. 4 and 5 apply to TBC systems with an oxide layer having a thickness of 3 μm and without the inclusion of friction between the crack surfaces.

In brittle materials, the most likely crack growth mechanism is mode I growth, which is initiated as K_I reaches the mode I fracture toughness K_{Ic} (Ref 9). For an air plasma-sprayed TBC, K_{Ic} is, based on the data of Evans et al. (Ref 10), reported to fall in the range 0.1 MPa · m$^{1/2}$ < K_{Ic} < 1 MPa · m$^{1/2}$. For central cracks (Fig. 4a) with a half-crack length in the interval 40 μm < a < 100 μm and for a > 140 μm, K_I during the first loading cycle exceeded 0.1 MPa · m$^{1/2}$. This implies the possibility of mode I crack growth during the first thermal cycle, assuming that K_{Ic} = 0.1 MPa · m$^{1/2}$. In the interval 100 μm < a < 140 μm, mode I propagation would take place at a later cycle, but prior to the steady state, because K^{ss}_{Imax} > 0.1 MPa · m$^{1/2}$. If K_{Ic} ≥ 0.3 MPa · m$^{1/2}$, approximately, mode I fracture will not occur for the range of crack lengths investigated.

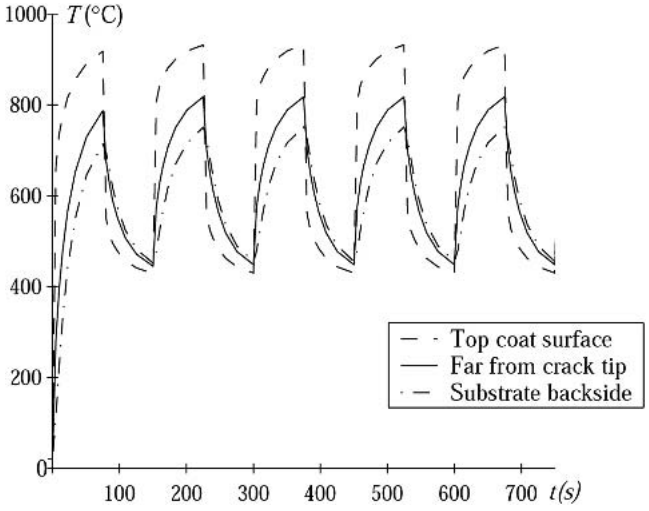

Fig. 3 Simulated thermal shock test cycles

For an edge crack of length a (Fig. 5a), K_I is largest during the first thermal cycle, and if a > 10 μm, approximately, K^1_{Imax} > K_{Ic}, assuming that K_{Ic} = 0.1 MPa · m$^{1/2}$, and, thus, fracture will occur. However, K^1_{Imax} never exceeds 0.5 MPa · m$^{1/2}$, and if K_{Ic} > 0.5 MPa · m$^{1/2}$, an edge crack in the interval length investigated will not propagate. Furthermore, by comparison of Fig. 4(a) to 5(a), it can be seen that the magnitude of K_I for an edge crack exceeds that of the corresponding central crack, regardless of crack length. This implies that an edge crack always constitutes a larger threat to the durability of the coating than does a central one.

The influence of crack tip position in relation to the undulation of the interface on the mode I stress-intensity factor is also seen from Fig. 4(a) and 5(a). The mode I stress-intensity factors are, generally speaking, larger for cracks with a crack tip position above a valley of the wavy interface for both crack configurations. Therefore, these cracks are more prone to propagation, whereas cracks are more likely to be stable when the crack tip positions are close to an apex. This result is in agreement with the calculation by Karlsson et al. (Ref 11) in which zones of compression are found in the vicinity of an apex between the topcoat and the bond coat. For a central crack, the magnitude of K^{ss}_{Imax} tends to increase with length. Thus, the longer the crack, the more unstable it is.

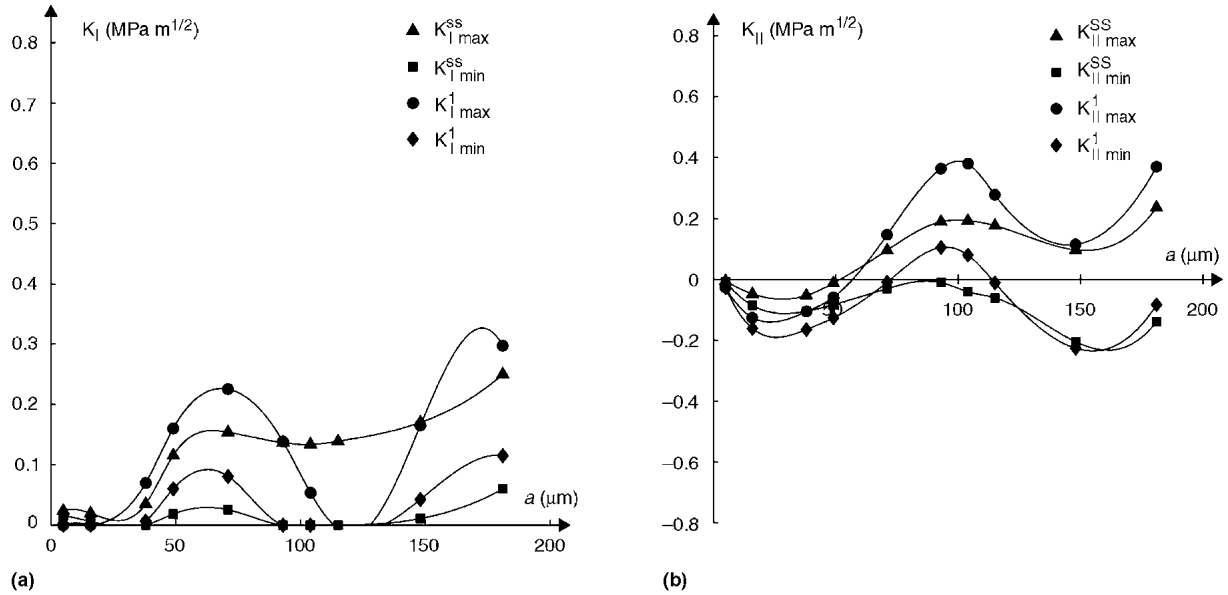

Fig. 4 Maximum and minimum values of (a) K_I and (b) K_{II} during the first load cycle and at steady state for central cracks of lengths 2a. The oxide layer thickness is 3 μm.

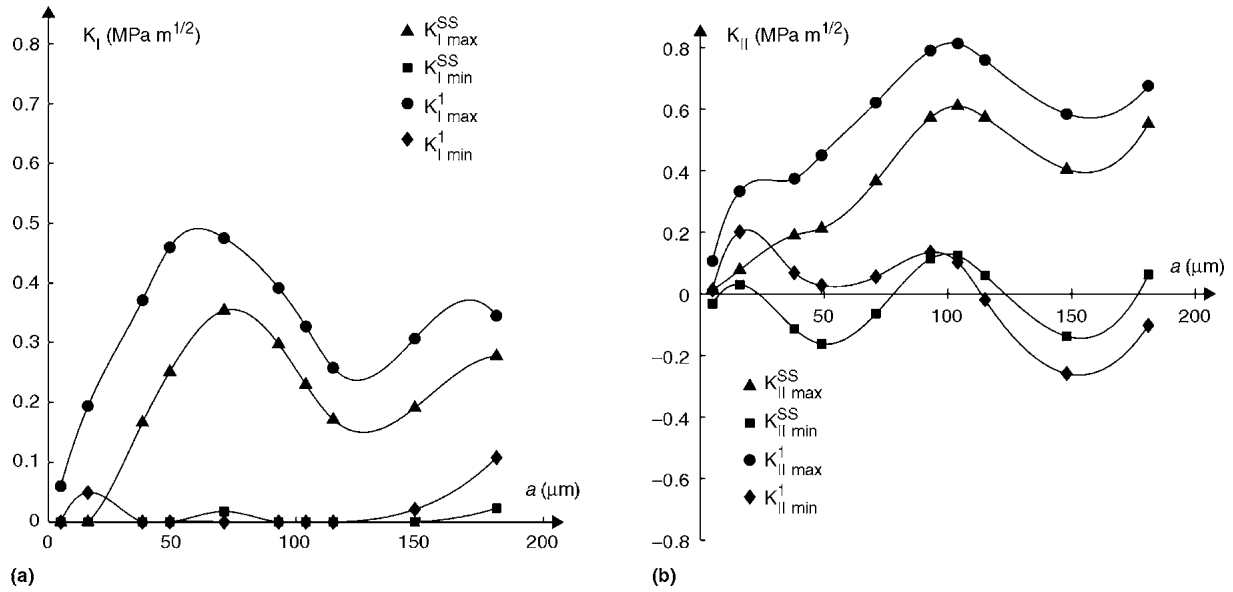

Fig. 5 Maximum and minimum values of (a) K_I and (b) K_{II} during the first load cycle and at steady state for edge cracks of lengths a. The oxide layer thickness is 3 μm.

The magnitudes of the mode II stress-intensity factors exceed those of mode I for a given a, as seen in Fig. 4(b) and 5(b). It is also seen that the magnitudes in the cases of edge cracks exceed the corresponding values for central cracks. The large magnitudes of K_{II} might imply mode II fracture, even though the mode II fracture toughness K_{IIc} exceeds that of K_{Ic}. According to Evans et al. (Ref 10), K_{IIc} is in the range 3 to ~5 MPa · $m^{1/2}$, so that a mode II fracture would not be initiated for the crack lengths investigated here. If mode I propagation is initiated, the mode II component will influence the crack propagation direction, so that the crack turns toward perpendicular to the largest principal stress. As the crack turns, the stresses will redistribute and, in order to determine whether or not the crack will continue to propagate, the actual crack path must be followed incrementally through the loading cycles. This is, however, beyond the scope of this study. Moreover, the change in the direction of the crack due to the mode II component might induce crack face contact, which could retard the crack propagation.

The results presented in this study apply to calculations without the inclusion of friction between the crack faces in the case of contacting crack surfaces. An investigation including Coulomb friction, with a coefficient of friction of 0.5 between the crack faces whenever they were in contact, did not significantly alter the magnitudes of the mode I stress-intensity factors. For mode II factors, however, friction decreased K_{II}, as expected, by hindering the possibility of crack face sliding. Because friction is always present, this means that mode II fracture becomes even less likely than mode I fracture.

The instant crack shapes, such as K_{Imax} and K_{Imin}, that are reached during the first load cycle and at steady state are shown in Fig. 6 and 7. Figure 6 applies to central cracks with half crack lengths a = 70 μm and a = 150 μm, and Fig. 7 applies to edge cracks of crack lengths a = 70 μm and a = 150 μm. These two crack lengths were chosen to represent cracks with a crack tip position above a valley of the wavy interface, which is believed to cause more unstable cracks. Compared to Fig. 2, the ordinate represents the crack face displacements in the y-direction, whereas the abscissa represents the crack length. As seen from the figures, the shorter cracks always are displaced more in the y-direction than in the longer ones. This is due to the higher thermally insulating effect from the crack faces for the longer cracks. The calculations show that the maximum values of K_I, both during the first temperature cycle and at steady state, are reached approximately 10 to 15 s after the maximum temperature is reached at the coating surface. The minimum values of K_I are reached approximately 5 s after the start of a thermal cycle. A comparison between Fig. 6(a) and (c) and Fig. 7(a) and (c) revealed that edge cracks open more than central cracks during the heating stage. This is consistent with the larger K_I values for edge cracks.

The initial crack configurations are sharp, with planar surfaces (Fig. 2). During thermal cycling, however, the crack surfaces become curved. This is probably due to the undulation of the wavy interface. If the crack has started to propagate during heating, roughness closure during cooling could occur and cause the crack to retard. Thus, the crack could be safe in the topcoat during thermal cycling even if it is relatively long. This observation supports the suggestion that threatening delamination in plasma-sprayed TBCs appears to accumulate by the progressive link-up of multiple short cracks rather than by the monotonic advance of one single dominant crack (Ref 3).

The effect on the stress-intensity factors of the presence of TGO also has been investigated. For the TBC system without inclusion of the TGO, the magnitude of the mode I stress-intensity factor reaches the maximum for cracks with a crack tip position very close to the apices of the interface, whereas K_I is lower for those with a crack tip position above a valley (Ref 5). When including TGOs, the opposite result is obtained, as seen from Fig. 4(a) and 5(a). The peak value of K_I occurs for cracks with a crack tip above a valley.

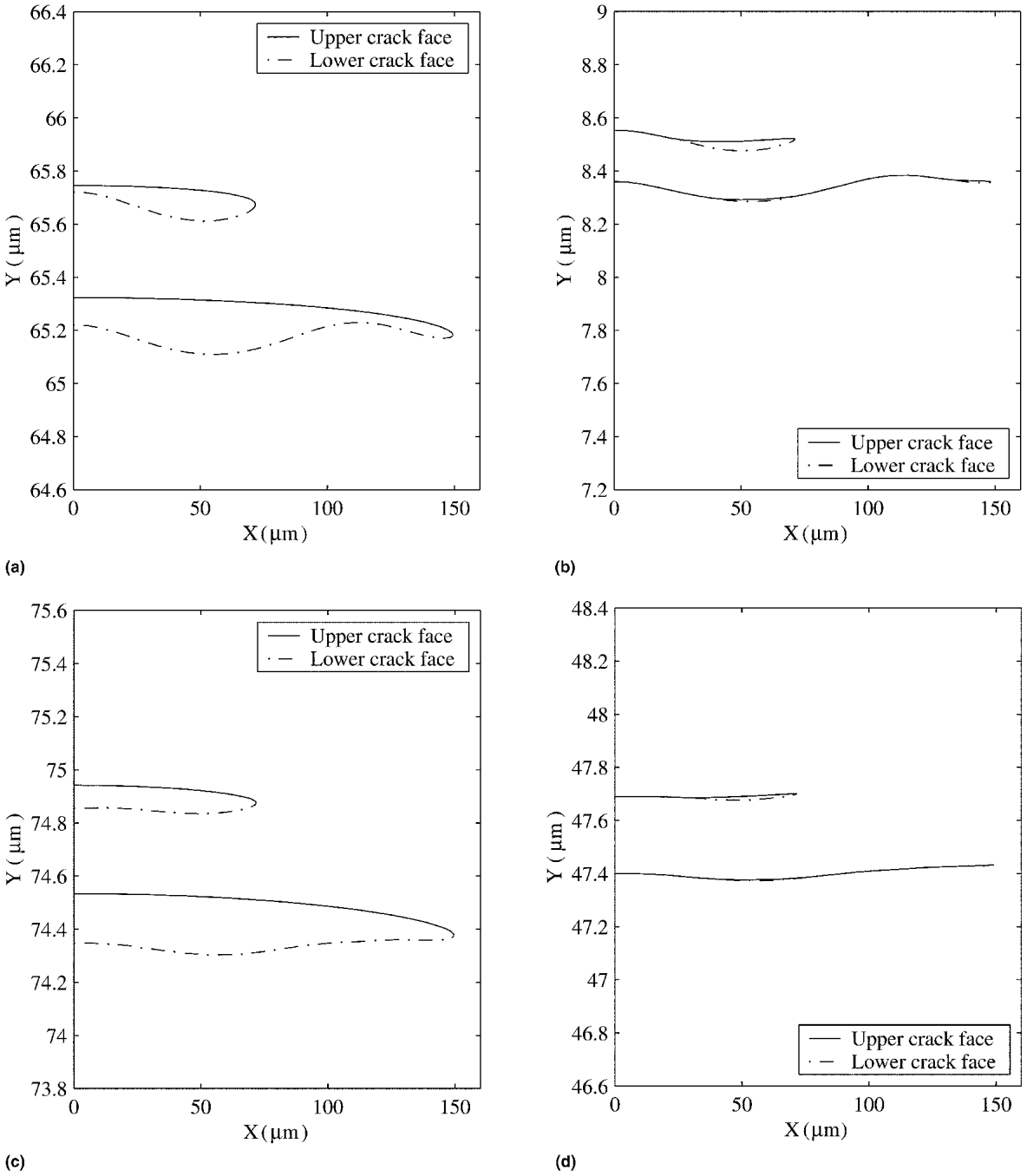

Fig. 6 Instant crack shapes for two central cracks of half-crack lengths a = 70 μm and a = 150 μm at (a) K^{1}_{Imax}, (b) K^{1}_{Imin}, (c) $K^{\mathrm{ss}}_{\mathrm{Imax}}$, and (d) $K^{\mathrm{ss}}_{\mathrm{Imin}}$. The oxide layer thickness is 3 μm.

Therefore, a central crack with half-crack length a = 70 μm and an edge crack with crack length a = 70 μm, representing a crack with a crack tip position above a valley, were selected to investigate the effect of TGO thickness. The corresponding stress-intensity factor ranges are shown in Fig. 8. For the central crack, the left group {A, B, C} in Fig. 8 applies, with A corresponding to the case without oxidation, B holding a 3 μm thick oxide layer, and C holding a 6 μm thick oxide layer.

For the edge crack, the right group {A, B, C} in Fig. 8 applies. As seen from Fig. 8, an increase in TGO thickness results in an increase in the magnitudes of the stress-intensity factor ranges for both modes I and II, irrespective of crack configuration. With an increase in TGO thickness, the trend toward crack closure decreases, as seen from Fig. 8(a) and (c) in which, for cases with $K_{\mathrm{Imin}} > 0$, no closure occurs so that the crack is open at the tip during the entire load cycle.

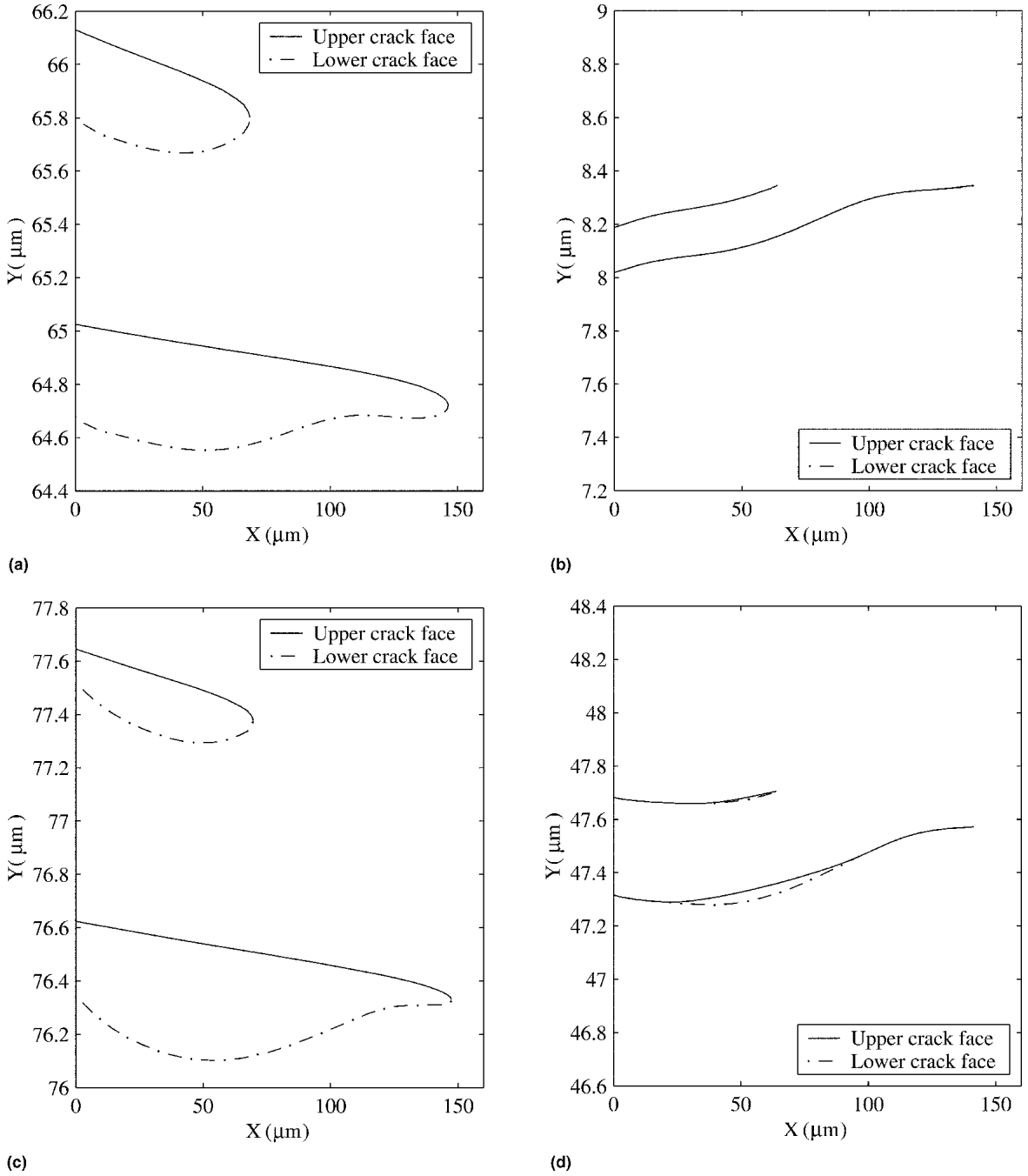

Fig. 7 Instant crack shapes for two edge cracks of lengths a = 70 μm and a = 150 μm at (a) K^{l}_{Imax}, (b) K^{l}_{Imin}, (c) K^{ss}_{Imax}, and (d) K^{ss}_{Imin}. The oxide layer thickness is 3 μm.

4. Conclusions

The risk of crack propagation from short inherent cracks in plasma-sprayed TBCs has been shown to be influenced by TGO thickness, crack configuration, crack tip position, and interfacial undulation. The eventual propagation of an edge crack occurs during the first load cycle, whereas for a central crack, the crack tip position plays an important role. A crack with a crack tip position close to a valley of the interface between the topcoat and the bond coat is more prone to propagation than a crack with a crack tip position above an apex. It was also found that an edge crack constitutes a greater threat to coating durability than a central crack due to the higher magnitude of the stress-intensity factor. Roughness closure of the crack faces during the cooling stage due to interfacial undulation could cause crack retardation and, thus, increase the fracture resistance of the TBC.

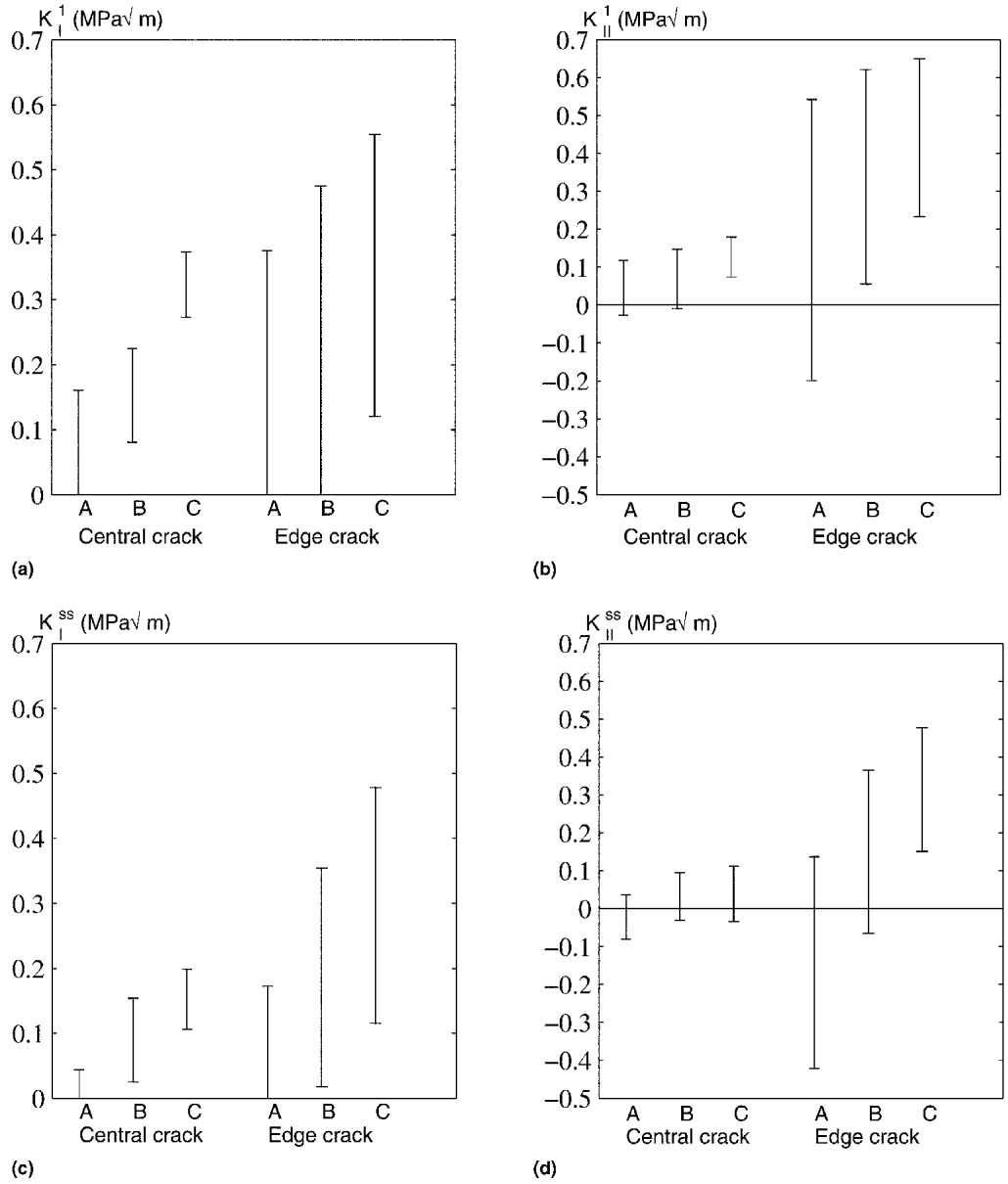

Fig. 8 The magnitude of the stress-intensity factor range of (a) K_{I}^{1}, (b) K_{II}^{1}, (c) $K_{\mathrm{I}}^{\mathrm{ss}}$, and (d) $K_{\mathrm{II}}^{\mathrm{ss}}$ for a central crack with a half-crack length $a = 70$ μm and an edge crack with crack length $a = 70$ μm for: case A, without oxidation; case B, with a 3 μm oxide layer thickness; and case C, with a 6 μm oxide layer thickness.

References

1. J.T. DeMasi, K.D. Sheffler, and M. Ortiz, Thermal Barrier Coating Life Prediction Model Development: Phase I-Final Report, NASA CR-182230, National Aeronautics and Space Administration, Washington DC, 1989
2. Y. Liu, "Life Modelling of Thermally Cycled Thermal Barrier Coatings, Licentiate Dissertation," ISRN LUTFD2/TFMT - 00/1005 - SE (1-66), Division of Materials Engineering, Department of Mechanics and Materials, Lund University, SE - 221 00, Lund, Sweden, May 2000
3. J.T. DeMasi, K.D. Sheffler, and S. Bose, Mechanisms of Degradation and Failure in a Plasma Deposited Thermal Barrier Coating, *J. Eng. Gas Turbine Power,* Vol 112, 1990, p 521-526
4. R.A. Miller, and C.E. Lowell, Failure Mechanisms of Thermal Barrier Coatings Exposed to Elevated Temperatures, *Thin Solid Films,* Vol 95, 1982, p 265-273
5. Y. Liu, C. Persson, and S. Melin, Fracture Mechanical Modeling of Thermal Shock Loading on Pre-cracked Thermal Barrier Coating Systems, *Thermal Spray 2003: Advancing the Science and Applying the Technology,* B.R. Marple and C. Moreau, Ed., May 5-8, 2003 (Orlando, FL), ASM International, 2003, p 1553-1556
6. ABAQUS/Standard, Version 5.8, User's Manual, Hibbitt, Karlsson & Sorensen, Inc., Pawtucket, RI.
7. R.S. Barsoum, Application of Quadrastic Isoparametric Finite Elements in Linear Fracture Mechanics, *Int. J. Fract.,* Vol 10, 1974, p 603-605
8. J.K. Wright, R.L. Williamson, D. Renusch, B. Veal, M. Grimsditch, P.Y. Hou, and M.R. Cannon, Residual Stresses in Convoluted Oxide Scales, *Mater. Sci. Eng.,* Vol A262, 1999, p 246-255
9. S. Melin, Residual Stresses in Convoluted Oxide Seales, *Int. J. Fract.,* Vol 53, 1992, p 121-128
10. A.G. Evans, D.R. Mumm, J.W. Hutchingson, G.H. Meier, and F.S. Pettit, Mechanisms Controlling the Durability of Thermal Barrier Coatings, *Prog. Mater. Sci.,* Vol 46, 2001, p 505-553
11. A.M. Karlsson, T. Xu, and A.G. Evans, The Effect of the Thermal Barrier Coating on the Displacement Instability in Thermal Barrier Systems, *Acta Mater.,* Vol 50, 2002, p 1211-1218